Turkish Journal of Physics

http://journals.tubitak.gov.tr/physics/

Research Article

Turk J Phys
(2019) 43: 80 – 92
© TÜBİTAK
doi:10.3906/fiz-1808-22

Synthesis, characterization, and magnetic properties of nanosized $Zn_{0.5}Co_{0.5}Er_xFe_{2-x}O_4$ prepared by coprecipitation method

Zouheir BITAR[1,*], **Doaa EL-SAID BAKEER**[2], **Ramadan AWAD**[1]
[1]Department of Physics, Faculty of Science, Beirut Arab University, Beirut, Lebanon
[2]Department of Physics, Faculty of Science, Damanhour University, Damanhour, Egypt

Received: 14.08.2018 • **Accepted/Published Online:** 15.01.2019 • **Final Version:** 22.02.2019

Abstract: In the present work, the effect of doping zinc cobalt ferrite by different concentrations of Er^{3+} on structural, optical, and magnetic properties was studied. Nanosized $Zn_{0.5}Co_{0.5}Er_xFe_{2-x}O_4$ ($0 \leq x \leq 0.2$) was synthesized by the coprecipitation method. XRD analysis confirmed the formation of one phase face FCC spinel structure belonging to the Fd3m space group. TEM exhibited that the particle size decreased with the increase of Er^{3+} content, which is in agreement with XRD results. Two significant absorption bands from FTIR spectra were observed between 400 and 600 cm^{-1}. The band gap energy value obtained from UV-Vis increased with the increasing concentration of Er^{3+}. The decrease of g-value is well correlated with the variation of particle size. All the VSM spectra reveal superparamagnetic behavior. The saturation magnetization decreases continuously while coercivity decreases abruptly with the increase of Er^{3+} content. The results of this work show the possibility that zinc cobalt ferrite doped by erbium can be useful for magnetic resonance imaging as a biomedicine application.

Key words: Rare earth, coprecipitation, structural properties, magnetic properties, spinel nanoparticles

1. Introduction

Nanosized magnetic particles are promising materials for developing many specialized applications such as magnetic drug delivery, biomedicine, storage devices, and microwave devices [1–9]. Sumithra et al. [10] studied the benefit of cobalt ferrite in biotechnology and bioengineering applications. Kebede et al. [11] reported that nano ferrites can be used in electronic device applications. Estelrich et al. [12] reported the application of nanoparticles in biomedicine, depending on their crystalline size. Structural, magnetic, and optical properties of nanoparticles are affected by particle size, synthesis method, and type of dopant ions (metals and rare earth ions). For zinc cobalt ferrite, cations occupy tetrahedral (A) and octahedral (B) sites. The site occupancy is often represented by the chemical formula $(M^{2+}_{1-\delta}Fe^{3+}_{\delta})[M^{2+}_{\delta}Fe^{3+}_{2-\delta}]O^{2-}_4$, where the square brackets and parentheses denote B and A sites, respectively; M represents a divalent cation; and δ is an inversion parameter. To control the growth of $Zn_{0.5}Co_{0.5}Er_xFe_{2-x}O_4$ nanoparticles and to reduce the aggregation of particles, poly(vinyl pyrrolidone) (PVP) is added as a capping agent [13,14]. The particle size has an effect on the physical properties of nanoparticles. When the particle size is less than 100 nm, the magnetic structure and properties are changed. A movement in the domain wall will occur until the multiple domains are replaced by a single domain structure. This change leads to new phenomena of superparamagnetism, enhanced anisotropy, and spin canting [15]. In superparamagnetism, surface effects and finite size control the magnetic behavior

*Correspondence: zouheirbitar@hotmail.com

of nanoparticles [16]. Frenkel and Dorfman [17] first investigated the effect of nanoparticle size, where they verified that a particle of size less than a critical value of around 15 nm would be formed of a single magnetic domain. Magnetic properties of spinel ferrites can be improved by doping them with rare earth ions [18]. Ahmad et al. [19] studied the magnetic and structural properties of erbium-doped Li–Ni nano ferrites and found that saturation magnetization and coercivity decreased with increasing Er concentration. Tholkappiyan and Vishista [20] investigated the effect of Er doping on the magnetic and structural properties of magnesium ferrite, where they observed an increase in coercivity and saturation magnetization. Ahmad and Tholkappiyan found contradictory results when they doped Er ions to nano ferrites. Since the radius of Er^{3+} is larger than that of Fe^{3+} ions, small concentrations of Er^{3+} ($0 \leq x \leq 0.2$) were used to permit the rare earth ion to enter the spinel lattice [21,22].

In this work, we report the coprecipitation method for the preparation of nanosized Er^{3+} ion-substituted zinc cobalt ferrites. We also present some results concerning the effect of Er^{3+} ions on the structure and morphological, optical, and magnetic properties of nanosized $Zn_{0.5}Co_{0.5}Er_xFe_{2-x}O_4$ ($0 \leq x \leq 0.2$).

2. Experimental details

Single phase nanosized $Zn_{0.5}Co_{0.5}Er_xFe_{2-x}O_4$, with x varied between 0 and 0.2, were synthesized by the coprecipitation method. Initially, we dissolved stoichiometric amounts of $CoCl_2.6H_2O$, $ZnCl_2$, $ErCl_3.6H_2O$, and $FeCl_3 \bullet 6H_2O$ (purity >99%) in distilled water in separate beakers. We mixed the solutions together under constant stirring by using a magnetic stirrer. We add to the obtained mixture 3 g of PVP solution that was dissolved in 100 mL of distilled water to produce a chemically homogeneous material. The solution was stirred for a sufficient time. Nanoparticles were formed from the hydroxides of metals when the PH of the solution reached a value of 12.5 by adding NaOH (4 M) solution dropwise under constant stirring. To transform the hydroxides into spinel ferrites, the mixture was heated for 2 h at 333 K with constant stirring. To remove the impurities, the mixture was washed many times with warm distilled water. Collected particles were dried in a furnace at 373 K for 24 h. The obtained solid was ground into a powder and then calcined for 6 h at a temperature of 823 K.

The prepared $Zn_{0.5}Co_{0.5}Er_xFe_{2-x}O_4$ nanoparticles were characterized by XRD in the range of $10° \leq 2\theta \leq 80°$using a Bruker D8 advance powder diffractometer with Cu-Kα radiation ($\lambda = 1.54056$ Å). The particle morphology was examined using a JEOL JEM-100CX transmission electron microscope operated at 80 kV. The Fourier transform infrared (FTIR) spectrum was recorded on an FTIR 8400S Shimadzu spectrophotometer in KBr pellets. The UV-Vis absorbance spectrum of the prepared samples was investigated by using a Jasco-V-670-UV-visible spectrometer in a range of wavelengths from 250 nm to 600 nm. EPR measurements were recorded using an X-band (9.7 GHz) EPR spectrometer (Bruker, EMX) at room temperature, using a high-sensitivity standard cylindrical ER 4119HS resonator with 100 kHz modulation frequency. A vibrating sample magnetometer (VSM), Lakeshore 7410, was used at room temperature to investigate the magnetic properties of nanosized $Zn_{0.5}Co_{0.5}Er_xFe_{2-x}O_4$ ($0 \leq x \leq 0.2$).

3. Results and discussion

3.1. XRD analysis

Figure 1 shows the XRD patterns of the $Zn_{0.5}Co_{0.5}Er_xFe_{2-x}O_4$ nanosized samples with different concentration of Er^{3+}. The results confirm the formation of single phase $Zn_{0.5}Co_{0.5}Er_xFe_{2-x}O_4$ with a face-centered cubic

spinel structure, space group Fd3m. No additional phases from the starting or other materials were detected in the diffraction patterns. As seen in Figure 1, the diffraction peaks become broader and the intensity of the peaks decreases as the concentration of Er^{3+} increases. From XRD spectra, we determined the average crystallite size (D_{XRD}), the lattice parameter (a), the theoretical X-ray density (ρ_x), the dislocation density (δ), the jump length "L" of the A- and B-sites (L_A and L_B, respectively), and the specific surface area (S) using the following equations [23–26]:

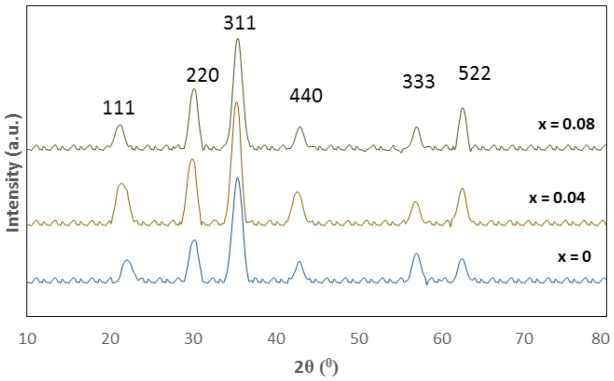

Figure 1. XRD patterns of nanosized $Zn_{0.5}Co_{0.5}Er_xFe_{2-x}O_4$ for (a) $x = 0$, (b) $x = 0.04$, (c) $x = 0.08$.

$$D_{XRD} = \frac{K\lambda}{\beta cos\theta}, \tag{1}$$

$$a = d_{hkl}\sqrt{h^2 + k^2 + l^2}, \tag{2}$$

$$\rho_x = \frac{8M}{Na^3}, \tag{3}$$

$$\delta = \frac{1}{D_{Xrd}^2}, \tag{4}$$

$$L_A = a\frac{\sqrt{3}}{4}, \tag{5}$$

$$L_B = a\frac{\sqrt{2}}{4}, \tag{6}$$

$$S = \frac{6}{\rho_x D_{Xrd}}, \tag{7}$$

where θ is the Bragg angle, λ is the X-ray wavelength, β is the full width at half maximum (FWHM) of the peak, k is a shape factor equal to 0.9 for spherical crystals with cubic unit cells, d_{hkl} is the interplanar lattice spacing, M is relative molecular mass, and N is Avogadro's number.

Table 1 displays that D_{XRD} decreases and a, ρ_x, δ, L_A, L_B, and S increase with the increase of Er^{3+} content. With increasing Er^{3+} concentration, the crystallite size decreases and this behavior can be explained

in two different ways. The first one is that the ionic radius of Fe^{3+} ions (0.645 Å) is smaller than that of Er^{3+} ions (1.004 Å), requiring more activation energy (higher strain) to replace Er^{3+} ions into octahedral sites for complete crystallization and grains formation. This is because the bond energy of Er-O is greater than that of Fe-O [27]. The second one is the crystalline anisotropy when different ionic radii of Er^{3+} and Fe^{3+} are substituted, leading to a reduction in the volume strain. Therefore, the crystallite size decreases with the increase of Er^{3+} content. Furthermore, the crystallite size decreases with increasing Er^{3+} concentration in order to minimize the volume strain. This result is in agreement with the results obtained by Chaudhari et al. [28] in $Ni_{0.5}Cu_{0.5}Zn_{0.5}La_xFe_{2-x}O_4$ nano ferrite. The increase of "a" confirms that the ionic radius of Er^{3+} is larger than that of Fe^{3+}. Since the increase of the lattice parameter is slight compared to the increase of the molecular mass, the X-ray density ρ_x increases. Lower values of δ show good crystallinity of $Zn_{0.5}Co_{0.5}Er_xFe_{2-x}O_4$ nano ferrite since δ gives the number of defects in the crystal. δ increases as "x" increases, indicating that Er^{3+} reduces the crystallinity of $Zn_{0.5}Co_{0.5}Er_xFe_{2-x}O_4$ nano ferrite. The increase of L_A and L_B can be attributed to the increase in the distance between the magnetic ions by increasing the concentration of large ions Er^{3+} at the B-sites, which has an effect on magnetic properties [29]. The specific surface area "S" of the particles is the summation of the areas of the exposed surfaces of the particles per unit mass. When the concentration of Er^{3+} was increased, S increased. The increase of S can be attributed to the decrease in particle size. There is an inverse relationship of particle size and density with surface area. The smaller the particle size, the larger the surface area.

Table 1. Values of crystallite size (D_{Xrd}) from XRD; particle size (D_{TEM}) from TEM; lattice parameter (a), X-ray density (ρ_x), dislocation density (δ), jump length of A-site (L_A), jump length of B-site (L_B), specific surface area (S), and band gap energy (E_g) from UV-Vis spectra; absorption bands wavenumber (ν_1 and ν_2); and Debye temperature (θ_D) from FTIR spectra for nanosized $Zn_{0.5}Co_{0.5}Er_xFe_{2-x}O_4$ ($0 \leq x \leq 0.2$) ferrite.

	$x = 0$	$x = 0.04$	$x = 0.08$	$x = 0.12$	$x = 0.2$
$\boldsymbol{D_{TEM}}$ (nm)	11.82	10.63	9.5	9.48	4.96
$\boldsymbol{D_{Xrd}}$ (nm)	12.28	11.26	11.05	10.92	8.275
$\boldsymbol{a}$ (Å)	8.372	8.383	8.385	8.388	8.415
$\boldsymbol{\rho_x}$ (g/cm$^{\mathbf{3}}$)	5.381	5.461	5.559	5.653	5.796
$\boldsymbol{\delta \times 10^{15}}$ **(lines/m$^{\mathbf{2}}$)**	6.631	7.887	8.189	8.386	14.603
$\boldsymbol{L_A}$ (Å)	3.6255	3.6302	3.6308	3.6322	3.6441
$\boldsymbol{L_B}$ (Å)	2.9602	2.9640	2.9645	2.9657	2.9754
$\boldsymbol{S}$ (m$^{\mathbf{2}}$/g)	90.785	97.560	97.673	97.192	125.084
$\boldsymbol{E_g}$ **(eV)**	3.02	3.04	3.06	3.08	3.14
$\boldsymbol{\nu_1}$**(cm^{-1})**	577.02	588.398	587.812	587.701	590.915
$\boldsymbol{\nu_2}$ **(cm^{-1})**	403.957	375.285	383.349	418.581	426.65
$\boldsymbol{\theta_D}$ **(K)**	705.32	692.88	698.26	723.51	731.62

3.2. TEM observation

TEM images of nanosized $Zn_{0.5}Co_{0.5}Er_xFe_{2-x}O_4$ are given in Figure 2. It is clear that the shape of the particles is spherical. From Table 1, the particle size (D_{TEM}) decreases with the increase of Er^{3+} concentration. This result is in good agreement with that obtained by XRD measurements. The particle sizes measured from

TEM are slightly less than the crystallite sizes calculated using Scherrer's formula from XRD.

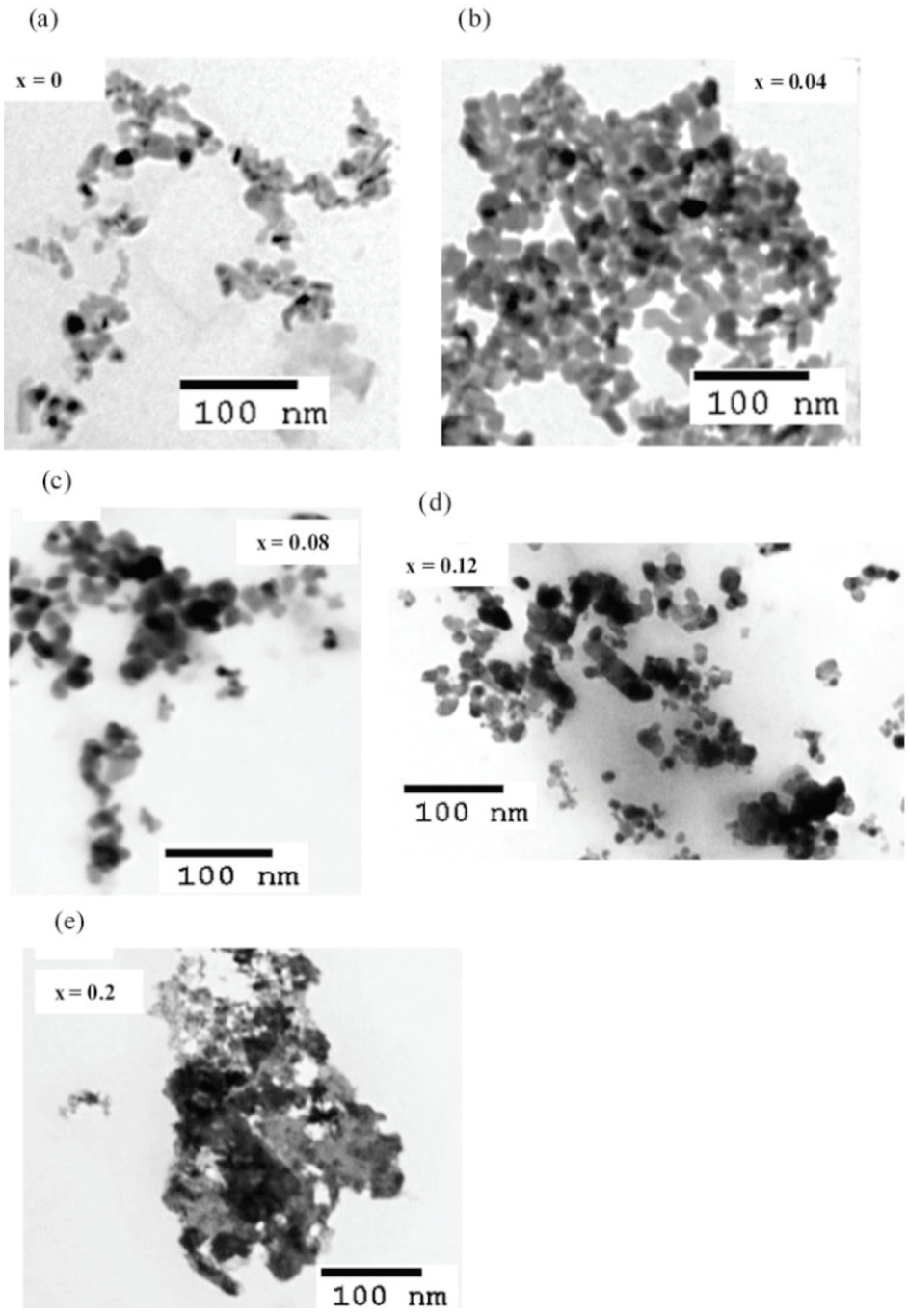

Figure 2. TEM images of nanosized $Zn_{0.5}Co_{0.5}Er_xFe_{2-x}O_4$ $(0 \leq x \leq 0.2)$.

3.3. FTIR analysis

FTIR spectra of nanosized $Zn_{0.5}Co_{0.5}Er_xFe_{2-x}O_4$ were recorded at room temperature in the range of 350–4000 cm^{-1}, and the spectra are represented in Figure 3. The FTIR spectra of all samples show the two main

absorption bands in the range of 350–700 cm^{-1}. These two vibration bands are related to intrinsic stretching vibrations of the metal at tetrahedral $M_{tet} \leftrightarrow O$ and octahedral $M_{oct} \leftrightarrow O$ sites. The band that appears at the higher wave number (ν_1, 500–600 cm^{-1}) corresponds to the tetrahedral complexes, while the band that appears at lower wave number (ν_2, 400–460 cm^{-1}) is assigned to the octahedral complexes [30]. The difference between ν_1 and ν_2 band positions can be attributed to the difference in the Fe^{3+}–O^{2-} distance for the octahedral and the tetrahedral sites by introducing Er^{3+} content [31]. The broadening of the ν_2 band is observed in $Zn_{0.5}Co_{0.5}Fe_2O_4$ doped with the rare earth element, suggesting the occupancy of rare earth ions on the B-sites [32]. The peaks between 1620 and 1650 cm^{-1} represent C=O stretching vibrations. A broadband between 3000 and 3600 cm^{-1} is observed, which corresponds to a stretching hydroxyl (O-H) group, representing the presence of water as moisture. The observed peak around 2330–2358 cm^{-1} corresponds to C–H bond stretching [33]. The Debye temperature θ_D can be calculated from the following relation [34]:

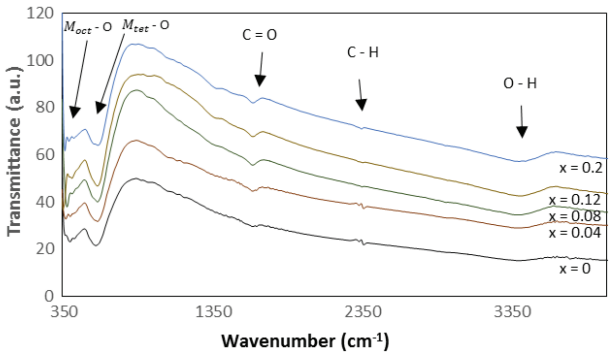

Figure 3. FTIR spectra of nanosized $Zn_{0.5}Co_{0.5}Er_xFe_{2-x}O_4$ $(0 \leq x \leq 0.2)$.

$$\theta_D = \frac{hc\nu_{av}}{k}, \tag{8}$$

where ν_{av} is the average value between ν_1 and ν_1, h is the Plank constant, k is the Boltzmann constant, and $c$is the velocity of light. The calculated values of the Debye temperature are listed in Table 1. Tatarchuk et al. [35] reported that the Debye temperature value of $Zn_{0.5}Co_{0.5}Fe_2O_4$ is 644 K. It can be noticed that all values of the Debye temperature vary between 705 and 732 K. These values have great importance in determining the conduction mechanism of these ferrites. It can be seen that θ_D decreases for $0 \leq x \leq 0.04$, and then it increases with increasing Er^{3+} content ($x > 0.04$). This behavior can be discussed based on specific heat theory [36]. According to this theory, electrons absorbed part of the heat and θ_D may change, and this suggests that the conduction for these samples is due to electrons (i.e. n-type or p-type). This means that the electronic contribution is predominant over the lattice vibration contribution.

3.4. UV-vis analysis

The optical absorption spectra of nanosized $Zn_{0.5}Co_{0.5}Er_xFe_{2-x}O_4$ were recorded using a UV-Vis spectrophotometer. Figure 4 shows the absorption spectra of the undoped and doped nanocrystals with different concentration of Er^{3+} in the 250–600 nm wavelength range. The band gap of the synthesized nanosized $Zn_{0.5}Co_{0.5}Er_xFe_{2-x}O_4$ is determined by means of the absorption spectrum. When the energy of an incident photon is larger than the band gap energy (E_g), the electrons can transfer from the valence band to the con-

duction band, causing an abrupt increase in the material absorbency corresponding to the wavelength that is related to E_g. Tauc's relation was used to determine the band gap energy of the prepared samples:

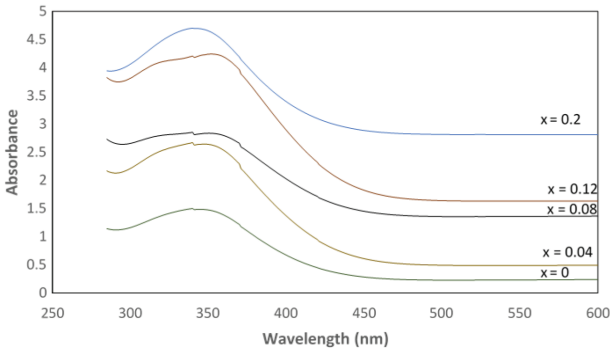

Figure 4. UV-Vis spectra of nanosized $Zn_{0.5}Co_{0.5}Er_xFe_{2-x}O_4$ $(0 \leq x \leq 0.2)$.

$$(\alpha h\upsilon)^n = A(h\upsilon - E_g), \tag{9}$$

where α is the absorption coefficient, $h\upsilon$ is the excitation energy, A is a constant, and n = 2 for a direct band gap, where the electron momentum is conserved. n = ½for indirect band gap material at which the momentum is not conserved [37,38]. By checking the linearity of the plot of $(\alpha h\upsilon)^2$ over a specified range of photon energies $h\upsilon$, it is possible to determine the optical band gap energy, as shown in Figure 5. The absorption coefficient (α) is calculated using the measured absorbance (A):

$$\alpha = 2.303\,\frac{A}{t}, \tag{10}$$

where t is the thickness of the sample. The values of E_g calculated for n = 2 are listed in Table 1. The values of E_g increase with the increase of Er^{3+} content, confirming the decrease of particle size for samples with higher Er content. The decrease in particle size can be explained by the quantum confinement effect [39,40]. The band gap values are similar to the band gaps of semiconductors, thus showing the semiconducting nature of the samples. The samples can be applied in photosensing applications [41].

3.5. EPR analysis

Figure 6 shows, at room temperature, the X-band EPR spectra for $Co_{0.5}Zn_{0.5}Er_xFe_{2-x}O_4$ with various Er^{3+} concentrations. A broad EPR signal was observed for $Co_{0.5}Zn_{0.5}Er_xFe_{2-x}O_4$ (with $0 \leq x \leq 0.2$) with a resonance magnetic field H_r shifted to greater values as the Er^{3+} concentration increased. The peak-to-peak line width (ΔH_{pp}) values, listed in Table 2, decrease with increased Er^{3+} concentration. This decrease can be attributed to the decrease in the dipolar interaction and increase in super-exchange interactions. The g-value is calculated from the resonance magnetic field H_r [42–44]. It is noticed from Table 2 that the value of g decreases from 2.815 to 2.248 with increasing Er^{3+} content up to $x = 0.2$. The super-exchange interaction between Fe^{2+} and Fe^{3+} at octahedral B sites can be the reason for the decrease in the g-value [45]. The spin–spin relaxation time constant T_2 is determined from the following equations [46]:

$$\frac{1}{T_2} = (g\beta\Delta H_{\frac{1}{2}})/\hbar, \tag{11}$$

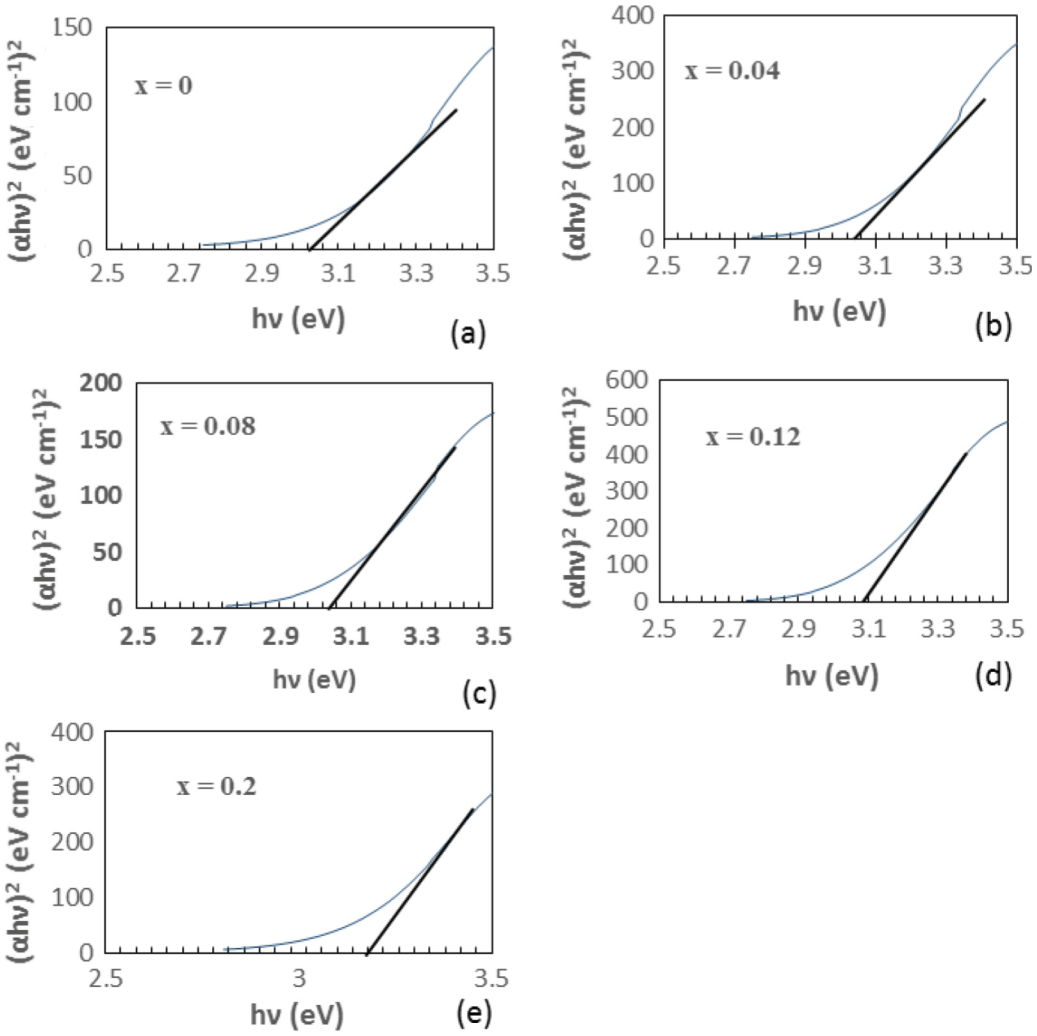

Figure 5. Tauc plot from UV-Vis spectra of nanosized $Zn_{0.5}Co_{0.5}Er_xFe_{2-x}O_4$ $(0 \leq x \leq 0.2)$.

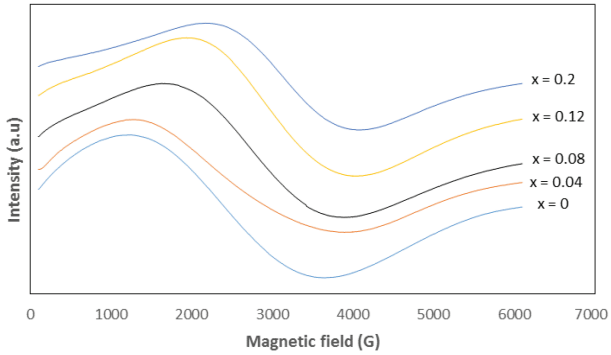

Figure 6. EPR spectra of nanosized $Zn_{0.5}Co_{0.5}Er_xFe_{2-x}O_4$ $(0 \leq x \leq 0.2)$.

$$\Delta H_{1/2} = \sqrt{3}\Delta H_{pp}, \tag{12}$$

Table 2. Values of g-factor, resonance field (H_r), peak to peak line width (ΔH_{pp}), line width at half of the absorption peak ($\Delta H_{1/2}$) spin–spin relaxation time constant (T_2) from EPR spectra, saturation magnetization (M_S), remnant magnetization (M_r), squareness ratio (M_r/M_s), coercivity (H_c), and magnetic moment (n_B) for nanosized $Zn_{0.5}Co_{0.5}Er_xFe_{2-x}O_4$ ($0 \leq x \leq 0.2$).

	$x = 0$	$x = 0.04$	$x = 0.08$	$x = 0.12$	$x = 0.2$
H_r (G)	2487	2498	2780	2956	3114
$\boldsymbol{\Delta H_{pp}}$ (G)	2499	2557	2187	2058	1888
$\boldsymbol{\Delta H_{1/2}}$ (G)	4328	4429	3789	3565	3271
g	2.815	2.802	2.518	2.368	2.248
$\boldsymbol{T_2}$ (s)	8.82×10^{-12}	8.66×10^{-12}	1.13×10^{-11}	1.27×10^{-11}	1.46×10^{-11}
$\mathbf{M_s}$ **(emu/g)**	50.232	45.245	43.234	39.03	24.981
$\mathbf{M_r}$ **(emu/g)**	0.393	0.165	0.100	0.205	0.091
$\mathbf{M_r/M_s}$	0.0069	0.0036	0.0023	0.0052	0.0036
$\mathbf{H_c}$ **(G)**	5.0701	2.4116	1.4738	3.7223	3.3288
$\boldsymbol{n_B}$ (μ_B)	2.13	1.96	1.91	1.75	1.16

where $\Delta H_{1/2}$ is the line width at half of the absorption peak. T_2 relates to how rapidly the magnetization in the plane perpendicular to the static magnetic field loses coherence. From Table 2, it is observed that the spin–spin relaxation time constant increases with the increase of Er^{+3} concentration. This behavior can be attributed to the enhancement of super-exchange interaction among magnetic ions through oxygen. Since the biological distribution of magnetic particles is significantly dependent on the crystallite size, the prepared samples can be used in magnetic resonance imaging (MRI) [47]. The high magnetic moments of Er^{3+} make it a good alternative to iron oxide T_2 contrast agents in high-field MRI, as even nonmagnetic ions have a noticeable effect when they replace Fe ions [48]. In our present work, an increase in T_2 was observed, which shows that doping zinc cobalt ferrite with erbium ions can improve the brightness of the image in MRI.

3.6. VSM analysis

Figure 7 shows the M-H loops of nanosized $Zn_{0.5}Co_{0.5}Er_xFe_{2-x}O_4$ with $x = 0$, 0.04, 0.08, 0.12, and 0.2. The measured saturation magnetization M_s, coercivity H_c, and remanent magnetization M_r, from M-H loops at room temperature in the range of –20 to 20 kG are listed in Table 2. The obtained values of saturation M_s, M_r, and H_c are reduced with the increase of Er^{+3} content. From Figure 7, we observe that the loops for the prepared samples that are measured at room temperature are very close ones, showing very low coercivity, which is considered to be typical superparamagnetic behavior. The decrease in M_s as particle size decreases can be attributed to the cation redistribution (exchange and substitution of cations in octahedral and tetrahedral sites). The redistribution of cations leads to a change in the structure of $Zn_{0.5}Co_{0.5}Er_xFe_{2-x}O_4$ from an inverse spinel to a mixed spinel [49,50]. Therefore, the surface behaves like a dead and inactive layer with slight magnetization [51]. The experimental values of magnetic moments n_B were calculated from the molecular weight (M_w) and the saturation magnetization (M_s) [52]. The values of n_B are listed in Table 2. Referring to Neel's model, A-A, B-B, and A-B super-exchange interactions in spinel ferrites exist. The change of cation distribution between A and B sites causes the variation in A-B exchange interaction strength when Er^{3+} dopes the ferrite. This leads to a change in the M_s value. When Er^{3+} ions are introduced, some of the Fe^{3+} from

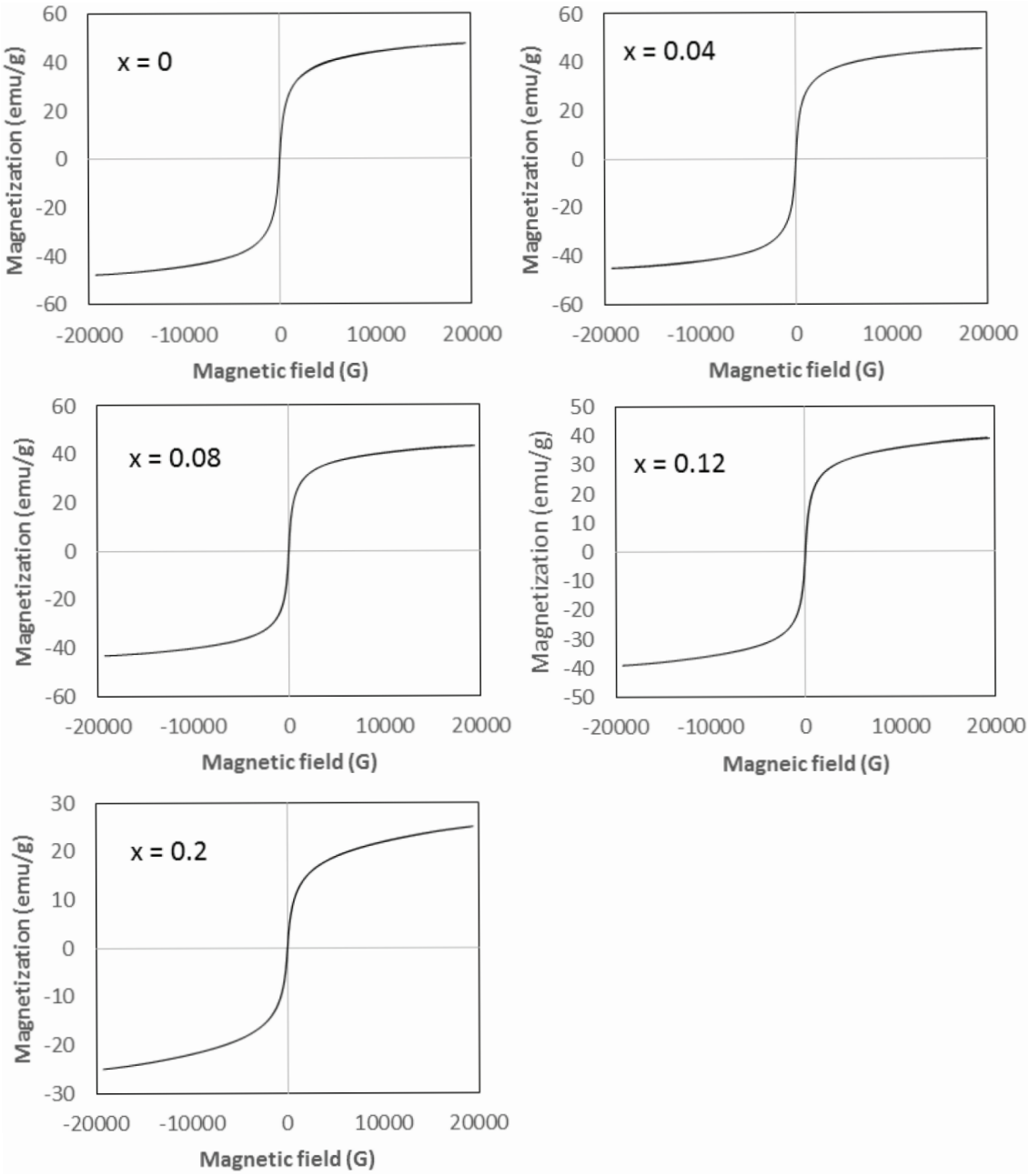

Figure 7. M-H curves of nanosized $Zn_{0.5}Co_{0.5}Er_xFe_{2-x}O_4$ $(0 \leq x \leq 0.2)$.

B-sites migrate to A-sites, which leads to the decrease of Fe^{3+} concentration at A-sites. Er^{3+} probably enters the octahedral site due to its large radius and the small tetrahedral A-site gap. The B-B exchange interaction at the octahedral site is reduced as a result of the decrease of Fe^{3+} concentration, which in turn reduces the A-B super-exchange interaction, too, which causes canting spins at the surface of nanoparticles. Therefore, the net magnetic moment $n_B = M_B - M_A$ will decrease (M_A and M_B are the B and A sublattice magnetic moments in μ_B) and result in a decrease in saturation magnetization, which is in agreement with the measured values that are listed in Table 2. The decrease of M_s with the decrease in particle size can be attributed to

the following: the magnetization of the octahedral sublattice is antiparallel to that of the tetrahedral sublattice in the ferromagnetic ferrite structure, and the noncollinear magnetic structure on the surface layer is observed in the case of ultrafine ferrites. An increase occurs in the proportion of noncollinear magnetic structure in which the magnetic moments are not aligned with the direction of the external magnetic field because of the reduction in particle size. This increase causes a decrease in the saturation of magnetization. The values of squareness ratio M_r/M_s for the prepared samples, listed in Table 2, are less than 0.5, which indicates the uniaxial anisotropy contribution produced by internal strains [53], or the formation of multidomain structure in the material. The coercivity values (H_c) and the squareness ratio for samples doped with the rare earth element (Er^{3+}) are smaller than those for the pure sample, as listed in Table 2. The values of coercivity and the squareness ratio are decreasing abruptly due to different concentrations of Er^{3+}; they decrease for $0 < x < 0.08$, then increase for $x = 0.12$ and decrease again for $x = 0.2$. This behavior shows an intense lattice distortion due to Er^{3+} substitution because of the influence of coercivity by many factors, such as particle size, the anisotropy of the crystal, and the magnetic domain structure [54]. The increase in coercivity for $x = 0.12$ can be attributed to the creation of more pinning sites. In a multidomain structure, the magnetization reversal arises from the domain wall movement. The domain walls are pinned at grain boundaries when they move through a particle. Therefore, the doping of the rare earth element creates more pinning sites and increases the coercivity of the ferrites [55].

4. Conclusions

In our study, we found that the coprecipitation method is efficient for the synthesis of $Zn_{0.5}Co_{0.5}Er_xFe_{2-x}O_4$ ($0 < x < 0.2$). XRD analysis has shown that the prepared nano ferrites were formed in the FCC single phase with an average crystallite size ranging from 8.27 to 12.28 nm. FTIR spectra show that the absorption bands corresponding to the tetrahedral and octahedral sites slightly shifted with increasing Er^{3+} content. The shifts in the bands are due to the perturbation occurring in the Fe^{3+}-O^{2-} band by Er^{3+} substitution. From UV-Vis absorption analysis, the band gap energies varied from 3.022 to 3.14 eV. The g-value was decreased and the spin-spin relaxation and the resonance magnetic field were increased by increasing the concentration of Er^{3+}. Saturation magnetization, coercivity, and remanent magnetization from M-H loops at room temperature were decreased when Er^{3+} was doped in zinc cobalt ferrite. The M-H loops analyses show the superparamagnetism behavior of the prepared samples. The results reveal that the rare earth ion Er^{3+}, doped in zinc cobalt ferrites, is a good candidate for biomedicine applications such as MRI due to the superparamagnetic nature and the improvement in the values of contrast agent T_2 with increasing Er^{3+} content.

Acknowledgment

Most of this work was done in the Materials Lab of the Physics Department, Faculty of Science, Beirut Arab University, Beirut, Lebanon, with the collaboration of the Physics Department of Alexandria University, Alexandria, Egypt.

References

[1] Gubbala, S.; Nathani, H.; Koziol, K.; Misra, R. *Condens. Matter* **2004**, *348*, 317-328.

[2] Sharifi, I.; Shokrollahi, H.; Amiri, S. *J. Magn. Magn. Mater.* **2012**, *324*, 903-915.

[3] Kappiyoor, R.; Liangruksa, M.; Ganguly, R.; Puri, I. *J. Appl. Phys.* **2010**, *108*, 094702.

[4] Schmid, G. *Nanoparticles: From Theory to Application*; Wiley: Weinheim, Germany, 2011.

[5] Jiles, D.; Lo, C. Sens. *Actuators A* **2003**, *106*, 3-7.

[6] Liangchao, L.; Haizhen, Q.; Yuping, W.; Jing, J.; Feng, X. *J. Rare Earths* **2008**, *26*, 558.

[7] Sim, S.; Miyajima, D.; Niwa, T.; Taguchi, H.; Aida, T. *J. Am. Chem. Soc.* **2015**, *137*, 4658-4661.

[8] Bolley, J.; Guenin, E.; Lievre, N.; Lecouvey, M.; Soussan, M.; Lalatonne, Y.; Motte, L. *Langmuir* **2013**, *29*, 14639-14647.

[9] Lee, J.; Huh, Y.; Jun, Y.; Seo, J.; Jang, J.; Song, H.; Kim, S.; Cho, E.; Yoon, H.; Suh, J. et al. *Nat. Med.* **2007**, 95-99.

[10] Sumithra, S.; Kishore, P.; Dhananjay, B.; Viendra, G. *Nanomedicine* **2018**, *13*, 1221-1238.

[11] Kebede, K.; Titus, M.; Bhekie, M. Mater. *Sci. Eng. B* **2017**, *215*, 37-55.

[12] Estelrich, J.; Sanchez-Martin, M. J.; Busquets, M.A. *Int. J. Nanomed.* **2015**, *10*, 1727-1741.

[13] Verma, R.; Mantri, B.; Ramphal; Srivastava, A. *Adv. Mater. Lett.* **2015**, *6*, 324-333.

[14] Kamari, H.; Naseri, M.; Saion, E. *Int. Nan. Lett.* **2014**, *4*, 118-129.

[15] Sohn, B.; Cohen, R. *Chem. Mater.* **1997**, *9*, 264-269.

[16] Batlle, X.; Labarta, A. *Appl. Phys.* **2002**, *3*, R15.

[17] Frenkel, J.; Dorfman, J. *Nature* **1930**, *126*, 274.

[18] Jie, S.; Lixi, W.; Naicen, X.; Qitu, Z. *J. Rare Earth* **2010**, *28*, 451.

[19] Ahmad, I.; Abbas, T.; Ziya, A.; Maqsood, A. *Ceram. Int.* **2014**, *40*, 7941-7945.

[20] Tholkappiyan, R.; Vishista, K. *Mater. Sci. Semicond. Process* **2015**, *40*, 631-642.

[21] Rezlescu, N.; Rezlescu, E.; Pasnicu, C.; Craus, M. *J. Phys. Condens. Matter* **1994**, *6*, 5707-5716.

[22] Al-Hilli, M.; Li, S.; Kassim, K. *J. Magn. Magn. Mater.* **2012**, *324*, 873.

[23] Vinuthna, C.; Ravinder, D.; Madhusudan, R.; Ravinder, D. *Int. J. Eng. Res. Appl.* **2013**, *3*, 654-660.

[24] Kumar, R.; Singh , R.; Barman, P. *Int. J. Sci. Eng. Res.* **2014**, *5*, 2229-5518.

[25] Kathirvel, P.; Manoharan, D.; Mohan, S.M.; Kumar, S. *J. Optocelectron. Biomed. Matter* **2009**, *1*, 25-33.

[26] Tholkappiyan, R.; Vishista, K. *Physica B* **2014**, *448*, 177-183.

[27] Peng, Z.; Fu, X.; Ge, H.; Fu, Z.; Wang, C.; Qj, L.; Miao, H. *J. Magn. Mag. Mat.* **2011**, *323*, 2413-2518.

[28] Chaudhari, V.; Shirsath, S. E.; Mane, M.; Kadam, R.; Shelke, S.; Mane, D. *J. Alloys Compd.* **2013**, *549*, 213-220.

[29] Mohamed, A.; Samy, A.; Tallat, M.; Saad, A.; Mohamad, A. *Turk. J. Phys.* **2005**, *29*, 163-177.

[30] Said, A.; Hemeda, D.; Abdel Kader, S.; Farag, G. *Turk. J. Phys.* **2007**, *31*, 41-50.

[31] Mohamed, R.; Rashad, M.; Haraz, F.; Sigmund, W. *J. Magn. Magn. Mater.* **2010**, *322*, 2058-2064.

[32] Hemeda, O.; Amer, A.; Aboul-Enein, S.; Ahmed, M. *Phys. Status Solidi A* **1996**, *156*, 29-38.

[33] Gharagozlou, M. *Prog. Color Color. Coat.* **2009**, *2*, 35-43.

[34] Waldron, R. *Phys. Rev.* **1955**, *99*, 1727-1735.

[35] Tatarchuk, T.; Bououdina, M.; Macyk, W.; Shyichuk, O.; Paliychuk, N.; Yaremiy, I.; Al-Najar, B.; Pacia, M. *Nanoscal. Res. Lett.* **2017**, *12*, 141.

[36] Mazen, S.; Abdel-Daiem, A. *Mater. Chem. Phys.* **2011**, *130*, 847-852.

[37] Oliva, F.; Avalle, L.; Santos, E.; Camara, O. *J. Photochem. Photobiol. A* **2002**, *146*, 175-188.

[38] Dressel, M.; Gruner, G. *Electrodynamics of Solids Optical Properties of Electrons in Matter*; Cambridge University Press: Cambridge, UK, 2002.

[39] Al-Hada, N.; Saion, E.; Shaari, A.; Kamarudin, M.; Flaifel, M.; Ahmad, S.; Gene, A *Mater. Sci. Semicond. Process* **2014**, *26*, 460-466.

[40] Amah, A. N.; Onoja, A.; Akpagher, R. *Turk. J. Phys.* **2013**, *37*, 289-295.

[41] Jain, R.; Gokhale, S. *International Journal for Innovative Research in Multidisciplinary Field* **2017**, *3*, 419-424.

[42] Pant, R.; Arora, M.; Kaur, B.; Kumar, V.; Kumar, A. *J. Magn. Magn. Mater.* **2010**, *322*, 3688.

[43] Wu, K.; Chang, Y.; Chen, H.; Yang, C.; Horng, D. *J. Magn. Magn. Mater.* **2004**, *278*, 156.

[44] Wu, K.; Huang, W.; Wang, G.; Wu, T. *Mater. Res. Bull.* **2005**, *40*, 1822-1831.

[45] Venkataraju, C.; Paulsingh, R. *Int. J. Nano Dimens.* **2015**, *6*, 255-261.

[46] Yadava, N.; Kumar, A.; Rana, P.; Rana, D.; Arora, M.; Pant, R. *Ceram. Int.* **2015**, *41*, 8623-8629.

[47] Bulte, J.; Kraitchman, D. *NMR Biomed.* **2004**, *17*, 484-499.

[48] Ho, D.; Sun, X.; Sun, S. *Acc. Chem. Res.* **2011**, *44*, 875-882.

[49] Jacob, J.; Abdul Khadar, M. *J. Appl. Phys.* **2010**, *107*, 114310.

[50] Shirsath, S.; Toksha, B.; Kadam, R.; Patange, S.; Mane, D.; Jangam, G.; Ghasemi, A. *J. Phys. Chem. Solids* **2010**, *71*, 1669-1675.

[51] Maaz, K.; Kari, S.; Mumtaz, A.; Hasanain, S.; Liu, J.; Duan, J. *J. Magn. Magn. Mater.* **2009**, *321*, 1838-1842.

[52] Yafet, Y.; Kittel, C. *Anti Phys. Rev.* **1952**, *87*, 290-294.

[53] Ammar, S.; Helfen, A.; Jouini, N.; Fievet, F.; Rosenman, I.; Villain, F.; Molinie, P.; Danot, M. *J. Mater. Chem.* **2001**, *11*, 186-192.

[54] Vasic, M.; Antic, B.; Kremenovic, A.; Nikolic, A. S.; Stoiljkovic, M.; Bibic, N.; Spasojević, V.; Colomban, P. *Nanotechnology* **2006**, *17*, 4877-4884.

[55] Gadkde, A.; Shinde, T.; Vasambekar, P. *Rare Met.* **2010**, *29*, 168-173.